2017

Deposition efficiency of barium hexaferrite by aerosol deposition

Scooter D. Johnson
U.S. Naval Research Laboratory, scooter.johnson@nrl.navy.mil

Douglas Schwer
U.S. Naval Research Laboratory

Dong-Soo Park
U.S. Naval Research Laboratory

Yoon-Soo Park
Korean Institute of Materials Science

Edward P. Gorzkowski
U.S. Naval Research Laboratory

Surface & Coatings Technology xxx (xxxx) xxx–xxx

Contents lists available at ScienceDirect

Surface & Coatings Technology

journal homepage: www.elsevier.com/locate/surfcoat

Deposition efficiency of barium hexaferrite by aerosol deposition

Scooter D. Johnson[a,*], Douglas Schwer[a], Dong-Soo Park[b], Yoon-Soo Park[b], Edward P. Gorzkowski[a]

[a] U.S. Naval Research Laboratory, Washington, D.C., United States
[b] Korean Institute of Materials Science, Changwon, South Korea

ARTICLE INFO

Keywords:
Ceramics
Nanoparticles
Gas flow
Aerosol deposition
Transfer efficiency
Barium hexaferrite
Fluid dynamics
Granule spray in vacuum

ABSTRACT

We present results of barium hexaferrite powder mass consumption across a wide range of starting powder quantities and deposition times. From these results we develop a transfer efficiency figure of merit to describe deposition efficiency and growth rates applicable to aerosol deposition and similar spray deposition techniques. We find that the transfer efficiency of barium hexaferrite was 0.082% and the transfer efficiency rate coefficient was 0.056 min^{-1} with a decay factor of −0.773. As a means to further understanding the deposition efficiency we present flow simulations of an aerosol deposition system using different particle sizes and standoff distances. We find that impact with the substrate strongly depends on the particle size, particle location within the nozzle, and standoff distance. We find that the values in the simulation are consistent with those used to produce films with the aerosol deposition system used at the Naval Research Laboratory and consistent with values found in the literature. We find that to improve the transfer efficiency nozzle design must be optimized, particle size must be carefully selected, standoff distance must be selected, and the powder in the aerosol chamber must be delivered at an optimal rate. These factors may be individually tuned to contribute to the final transfer efficiency figure of merit that can be used to assess the efficiency of the aerosol deposition process.

1. Introduction

Aerosol deposition (AD) is a technique that rapidly produces dense polycrystalline films that are several microns thick. One hallmark of AD is that the entire process occurs at room temperature, thus enabling integration of high-melting-temperature materials with low-melting-temperature materials. The process was developed in the late 1990s by Jun Akedo et al. [1] building on earlier work in the 1980s [2,3]. The application arena for AD films are numerous; some include, piezoelectrics [4], biomedical implants [5], abrasion coatings [6], electromagnetic interference shielding [7,8], rf circuitry [9], and corrosion resistance [10]. Additional background can be found in reviews of AD [11,12]. As AD develops from the laboratory scale to the industrial scale a detailed understanding of the system properties and mechanisms of the growth process become increasingly important for maximizing deposition efficiency and in tuning the parameters for each material growth. This motivates the need to develop a fundamental understanding of the process parameters and to develop a figure of merit (FoM) for comparison within the field of AD and between other spray deposition techniques.

There have been some efforts on simulating and measuring the gas and particle flow from nozzles in AD and cold spray. Gas and particle velocities for cold spray were estimated using an isentropic gas flow model that provides a framework for analytical calculations of gas velocities [13,14]. Reports specific to AD include an experimental apparatus to measure the impact velocity of 30–70 nm silver particles and Pb-Zr-Ti-O (PZT) particles. The velocities were found to be 650 m/s and 200 m/s, respectively indicating that ceramic particles require much less velocity to deposit than metallic particles [15]. Estimates of the impact velocity based on the carrier gas were also reported to vary between 150 and 500 m/s for α-Al_2O_3 and PZT particles [12]. More recent work using numerical simulation of Al_2O_3 particles between 0.5 and 15 μm in size suggests that particle velocity can be tuned both by the particle size and pressure in the deposition chamber [16]. Simulations of gas flow using different nozzle sizes, chamber pressures, and substrate standoff distances also suggest the importance of tuning these parameters to optimize the gas flow [17]. Later, these parameters were correlated with experimental results of deposition of 3 μm diameter TiO_2 particles with a standoff distance of 15 mm [18]. More recently, computational fluid dynamic CFD simulations of gas flow with 0.5 μm diameter Al_2O_3 particles were performed for a range of standoff distances and pressures. They found that the average impact velocity of the particles were between 335 and 346 m/s for standoffdistances between 1 and 7 mm, respectively. They compared experimental results

* Corresponding author.
E-mail address: scooter.johnson@nrl.navy.mil (S.D. Johnson).

http://dx.doi.org/10.1016/j.surfcoat.2017.06.085
Received 24 March 2017; Received in revised form 9 June 2017; Accepted 11 June 2017
0257-8972/ Published by Elsevier B.V.

Nomenclature

A	Coefficient of transfer efficiency
AC	Aerosol chamber
AD	Aerosol deposition
BaM	Barium hexaferrite
C_s	Stokes drag coefficient
CFD	Computational fluid dynamic (simulation)
D	Diameter
DC	Deposition chamber
E	Total specific energy (internal plus kinetic)
FCT	Flux-corrected transport
FoM	Figure of merit
GSV	Granule spray in vacuum
I	Identity matrix
KIMS	Korean Institute of Materials Science
NRL	Naval Research Laboratory
P	Pressure
PZT	Pb-Zr-Ti-O compounds
Re	Reynolds number
T	Temperature
T	Thickness
TE	Mass transfer efficiency
f	High velocity correction term
l	Length
m	Mass
rf	Radio frequency
t	Time
v	Gas-phase velocity
w	Width
x	Longitudinal position
y	Axial position
β	Exponent of the time dependence of transfer efficiency
γ	Ratio of the specific heats
λ	Thermal conductivity
μ	Gas-phase viscosity
ρ	Density
τ	Viscous stress tensor

Subscripts and superscripts

$_b$	Boundary
$_f$	Final condition
$_{film}$	Properties pertaining to the film
$_i$	Initial condition
$_j$	Particle index in simulation
$_p$	Particle
$_{rel}$	Relative
$_{stock}$	Spray feedstock
$_{sub}$	Substrate
$_{sweep}$	Nozzle sweep
$_{sym}$	Symmetric part of tensor
$'$	Effective value

that found that the film thickness decreased with increasing standoff distance [19]. These efforts suggest that particle type, particle size, chamber pressure, nozzle design, and standoff distance all play an important role in understanding and controlling the deposition process.

There has been very little reported on the effect of powder mass flow through the nozzle. Studies of milling and heat treatment of the powders have been done [20,21], however no fundamental study of the mass flow in AD systems has been found in the literature. In this work, we report experimental results that relate powder mass consumption and film thickness and we use these results to develop a mass transfer efficiency FoM. We include results of simulations of particle flow near the substrate that suggest particle impact is strongly governed by standoff distance and particle size. We synthesize these results to suggest that the mass transfer rate is also an important parameter in film formation of AD systems.

2. Materials & methods

2.1. Numerical procedure

The numerical simulations focus on the particle paths as they pass through the nozzle and impinge on the substrate in the deposition chamber. Because of that, we only model the deposition chamber, as well as the channel between the aerosol chamber (AC) and deposition chamber (DC).

For these simulations, the volume fraction is assumed to be low enough that we have only one-way coupling of the gas-phase to the dispersed-phase. The gas-phase follows the viscous Navier-Stokes equations in conservative form for a compressible gas:

$$\frac{\partial \rho}{\partial t} + \nabla\cdot\rho v = 0$$

$$\frac{\partial \rho v}{\partial t} + \nabla\cdot\rho v \otimes v = -\nabla P + \nabla\cdot\tau$$

$$\frac{\partial \rho E}{\partial t} + \nabla\cdot(\rho E + P)v = \nabla\cdot\lambda\nabla \mathrm{T}$$

The viscous stress tensor, τ, is defined as

$$\tau = \mu(\nabla v)_{\mathrm{sym}} - \frac{2}{3}\mu(\nabla\cdot v)\mathbf{I}$$

The Sutherland expression is used for expressing viscosity as a function of temperature,

$$\mu(\mathrm{T}) = 1.458 \times 10^{-5}\left(\frac{\mathrm{T}^{3/2}}{110+\mathrm{T}}\right).$$

We assume the Prandtl number is 1 to calculate the thermal conductivity of the gas. To close these equations, we assume a calorically perfect gas and the ideal gas relation:

$$\rho E = \frac{P}{\gamma - 1} + \frac{1}{2}\rho v^2.$$

Single particles are tracked using a Lagrangian particle-tracking procedure. The particle is characterized by its mass $m_{p,j}$, diameter $D_{p,j}$, location $x_{p,j}$ and velocity $v_{p,j}$. The single-particle equation of motion is

$$m_{p,j}\frac{dv_{p,j}}{dt} = 3\pi D_{p,j}\mu(v - v_{p,j})f(\mathrm{Re}_{p,j})$$

where v is the gas-phase velocity, μ is the gas-phase viscosity, and $\mathrm{Re}_{p,j}$ is the Reynolds number based on the slip velocity, $v_{\mathrm{rel},j} = (v - v_{p,j})$. The high velocity correction term, $f(\mathrm{Re}_{p,j})$is the ratio of the actual coefficient of drag to the Stokes drag coefficient, $C_{s,j} = 24/\mathrm{Re}_{p,j}$ and has been the subject of extensive research. The simplest high velocity correction term is the Schiller and Naumann law [22], expressed as

$$f(\mathrm{Re}_{p,j}) = (1+0.15 \quad \mathrm{Re}_{p,j}^{0.687})$$

This correlation works well for Reynolds numbers under 800. For particles on the order of one micron, the Reynolds number will always be well below 800.

For the gas-phase, the flux-corrected transport (FCT) algorithm of Boris and Book [23] is used, which is especially suited for high-speed

flow. The version of the algorithm used for the results reported in this article is described in detail in NRL/MR/6410-93-7192 [24]. The current algorithm uses domain decomposition for computing the gas-phase [25]. This method is very efficient and scalable for explicit time-integration techniques such as the FCT algorithm. The geometry for the nozzle, substrate, and substrate mount is included using the Virtual-Cell-Embedding technique of Landsberg and Boris [26]. For the tracked particles, the 4th-order Adams-Bashforth and Adams-Molton predictor-corrector schemes are used for the time integration.

2.2. Simulation and experimental details

Simulation is based on the geometry of an AD system built at the Naval Research Laboratory (NRL), Washington, DC, USA and described in the literature [27,28]. Simulations were accomplished for a two-dimensional domain that included both the DC and the channel between the AC and DC. Two separate domains are used for the two regions, and then patched together at $x = 0$ mm. The solution domain goes from -94.7 mm (94.7 mm before the start of the deposition chamber) to 325 mm in the x-direction, and from $y = 0$ (centerline) to $y = 60.45$ mm at the top of the deposition chamber. The nozzle throat is at $x = 141$ mm, and the substrate is either 7.5 mm or 10 mm from the nozzle throat. The resolution at the nozzle throat is 0.2 mm and at the substrate is 0.05 mm. The grid dimension for the channel zone is 200×57, or 11,400 cells, and for the deposition chamber is 1627×293,or 476,711 cells. The full domain is shown in Fig. 1. The upstream stagnation pressure and temperature are held at 500 Torr, 300 K. The downstream back pressure is held at 1 Torr. The simulation is first run with the gas-phase only to create a steady-flow. Once this is set up, particles or tracers are placed in the channel at $x = 130$ mm (ahead of the throat), and are distributed in 0.25 mm intervals from the centerline to the outer wall of the channel. They are initialized with the gas-velocity at their respective location.

Powder consumption and deposition efficiency were found by depositing barium hexaferrite (BAM) *Trans-Tech, Inc., Adamstown, MD, USA* using a custom AD system at the Korean Institute of Materials Science (KIMS), Changwon, Gyeongnam, S. Korea and is described in the literature [29,30]. The BaM powder was heat treated at 1000 °C for 2 h. Powders were sieved to sizes below 106 μm using a number 140 size sieve mesh then weighed before loading into the AC to obtain the initial mass. The final mass was determined by weighing the remaining contents of the AC after each run. Each run was performed on glass using a 35 mm × 0.4 mm deLaval nozzle. The gas was medical grade dried air and was supplied through the AC at 10 lpm and through a supplementary line at 3 lpm as described in [30]. The standoff distance from the nozzle to the substrate was 10 mm. Films were measured at several points using a stylus profilometer and the average thickness was used in this study. The total deposition time was calculated from the number of sweeps based on the sweep length of 10 mm and sweep speed of 5 mm/min.

3. Results & discussion

3.1. Mass consumption

Fig. 2 is a plot of the final powder mass removed from the AC after the deposition run versus the initial powder mass loaded into the AC before the run. The data are for 41 depositions of BaM performed under identical conditions ranging from 2 to 32 min in deposition time as indicated by the colored points. The data show a correlation ($R^2 = 0.956$) between the starting and ending quantities of powder based on the linear fit line shown. The plot and good fit suggest a linear relationship between the amount of powder loaded into the AC and the amount that remains after the run. The slope of the fit line is 0.8 and on average, for all of the depositions performed, 64% of the BaM powder initially loaded into the AC remains after the deposition. This average is lower, but comparable to the slope of the fit line. The fit line can be interpreted as a broader measure of the powder consumption for BaM in this system, because it tracks consumption across many starting powder quantities and deposition times. In general, we might expect a slope to approach 1 for a system (or material) that has very little or no consumption and to approach 0 for a system that consumes all the powder in the AC. This relationship gauges consumption for this particular system material, but may be applied to other systems and materials as a basis for understanding powder consumption more generally in the AD process.

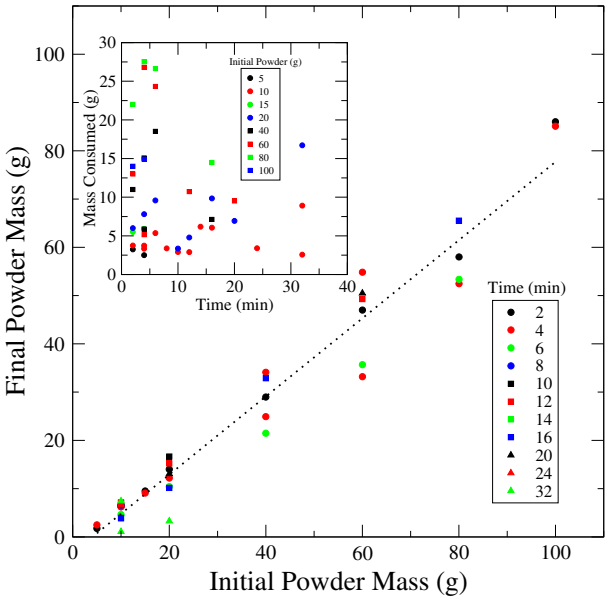

Fig. 2. A plot of the ending powder quantity removed from the AC versus the starting quantity loaded into the AC for several deposition. The dashed line is a linear fit to the data ($R^2 = 0.956$) suggesting that the powder consumption is relatively fixed regardless of the quantity of powder used. The different point colors and shapes indicate the time duration of each run. The inset is a plot of the powder consumption (initial powder mass minus final powder mass) versus time. The different point colors and shapes indicate the initial starting mass. The inset data show no apparent correlation between time and powder consumption. (For interpretation of the references to color in this figure legend, the reader is referred to the web version of this article.)

In this study the mass of the powder is used, but it may be worthwhile to add that loading the same amount of powder into a larger (or smaller) AC may produce different results. It is reasonable then to consider the volume of the AC (and possibly the volume of powder loaded into the AC) as a more accurate parameter related to powder

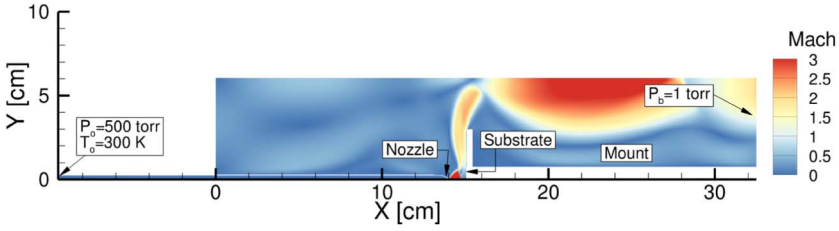

Fig. 1. Full domain solution for deposition chamber and channel. Spacing between nozzle and substrate is 10 mm.

consumption. While the volume of the AC (546 ml in this study) can be accurately measured, an accurate value of powder volume may be more difficult to obtain, since it depends on the packing density. Future work may include examining the powder consumption using various volume sizes of the AC.

The inset of Fig. 2 shows the mass consumption (initial powder mass minus final powder mass) plotted against time. The colored points indicate the initial powder quantity. Examining this plot we can find no apparent correlation between mass consumption and time for any of the initial powder quantities used. This result may be due to the manner in which the powder is agitated. In this process the powder is continually packed and unpacked against the walls of the AC [20]. If these processes are governed by random or chaotic behavior, we would not expect a simple time dependence in the mass consumption. It can also be observed in some systems that during the initial startup phase where the pressure in the AC goes from less than about 0.1 Torr to 300–500 Torr the powder goes through a turbulent pressure regime, which causes large amounts of powder to flow. It is possible that these plots largely reflect the powder loss during this initial start-up phase or during initial deposition sweeps.

Studies of mass consumption of different materials or of materials processing may add insight into the powder consumption of AD systems. Recently, granule spray in vacuum (GSV) has been developed to facilitate better powder flow in the AC and by utilizing a granule feeder system [29,30]. This approach may provide insight into the effect that packing has on the mass consumption and film formation. It should be stressed that maximizing powder consumption may not be the intended goal, instead one wishes to maximize the ratio of film mass to powder consumption. Ideally, every particle that exits the nozzle would impact the substrate and add to the film mass.

3.2. Deposition efficiency in AD systems

The deposition rate given in thickness per time is often used by researchers of film growth, such as pulsed laser deposition and atomic layer deposition where the entire substrate area is exposed to the process uniformly in time. This differs from techniques such as cold spray, plasma spray, and AD where the film is created by locally directing the deposition and sweeping across the substrate in time (see for example, Ref. [31]). Unfortunately, a deposition rate given as a thickness per time does not work as a good measure of deposition efficiency. As a simple example consider the deposition rate for a 5-μm-thick film deposited at a sweep rate of 1 mm/min. The deposition rate will be better if performed over a 1 mm length (5 μm/min) compared to a 10 mm length (0.5 μm/min) simply because the nozzle takes time to sweep longer distances. Perhaps a volume deposition rate would be a better measure of the deposition rate. This FoM is now a function of the nozzle width and length of scan. In this case, the lengths involved make it easy to obfuscate the true output of the system. For example, if a film were created that had a width and a length of 10 mm each and a thickness of 5 μm and a sweep rate of 1 mm/min the volume deposition rate would be 50 mm^2μ m/min. Now by changing the width or length of the film produced by only 1 mm the volume deposition rate improves to 55 mm^2μm/min. It can be readily seen how this FoM obscures the true nature of the deposition rate.

A better gauge of deposition efficiency may be borrowed from the spray paint industry. Spray painting has been used in the automotive industry for decades and substantial work has been devoted to standardizing the efficiency of spray coated parts and materials [32]. The transfer efficiency *TE* is a measure of how much of the starting material has adhered to the substrate. We adopt this terminology partially to make a distinction from the deposition rate as used above. The *TE* can be attained by comparing the change in mass of the coated part to the change in mass of the starting material in the spray reservoir.

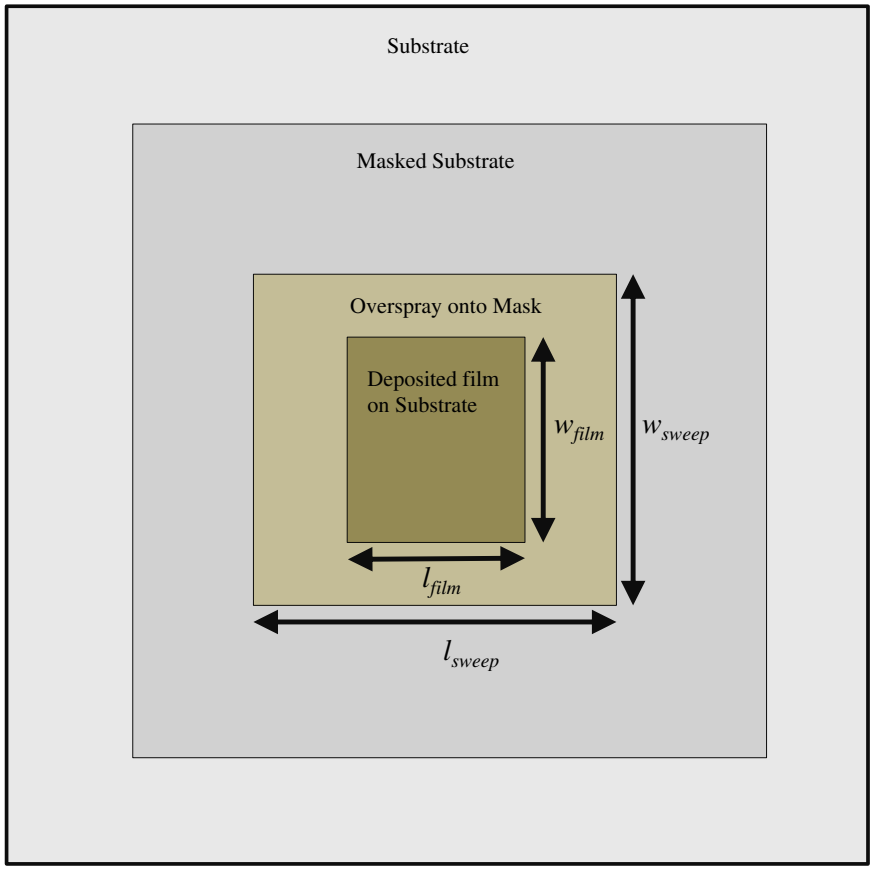

Fig. 3. A drawing of a typical masked film deposition in AD. The dark center rectangle of area $l_{film} \times w_{film}$ represents that actual film deposited through the mask. The lighter outer rectangle of area $l_{sweep} \times w_{sweep}$ represents the deposition overspray onto the masked region (shown in light grey).

Mathematically, we can write this relationship as

$$TE = \frac{m_f^{sub} - m_i^{sub}}{m_i^{stock} - m_f^{stock}} \times 100. \quad (1)$$

Here, m_f and m_i refer to the final and initial values of mass for the substrate (*sub*) and feedstock (paint or powder) (*stock*). An implicit assumption in Eq. (1) is that the entire substrate is exposed to the spray nozzle. In the case of substrate masking typically done in AD, a percentage of the coating mass is intentionally lost as shown in Fig. 3. The *TE* of such a film may be calculated by assuming that the properties of the overspray deposited onto the mask do not change significantly from the film deposited onto the substrate. The mass of the film is then corrected to the area of the overspray region as

$$m'_{film} = T_{film} \times l_{sweep} \times w_{sweep} \times \rho_{film}. \quad (2)$$

Here, T_{film} is the film thickness, l_{sweep} and w_{sweep} are the length and width of the nozzle sweep, respectively, and ρ_{film} is the density of the film. The *TE* for AD masked films can then be written as

$$TE_{AD} = \frac{m'_{film}}{m_i^{stock} - m_f^{stock}} \times 100 = \frac{T_{film} \quad l_{sweep} \quad w_{sweep} \quad \rho_{film}}{m_i^{stock} - m_f^{stock}} \times 100 \quad (3)$$

It can be noted that Eq. (3) may be used regardless of different nozzle sizes, sweep rates, sweep lengths, and sweep types such as rastering. It also incorporates film thickness and density, which are commonly measured film properties.

Fig. 4 is a plot of TE_{AD} and TE_{AD}/t calculated from Eq. (3) using the powder consumption data found in Fig. 2 that was performed with a 10 mm sweep length (l_{sweep}) and a 35 mm nozzle width (w_{sweep}). The film density is taken to be 5.04 g/cm^3 (95% of theoretical density).

The red points in Fig. 4 are TE_{AD} versus time. The data show that the TE_{AD} has a wide range in values from 0.045% to 0.142%. Inspection of the plot indicates that this improvement does not have a strong time dependence. Similarly, we do not find a strong dependence of TE_{AD} on m_f^{stock} or m_i^{stock} (data not shown). The average TE_{AD} for all of the films was 0.082% with a standard deviation of 0.026%.

The black points show TE_{AD} scaled by the deposition time TE_{AD}/t. The data collapse into a power law relationship as shown by the dashed fit line. Explicitly, the fit to the data is $TE_{AD}/t = 0.056t^{-0.773}$. The coefficient is a measure of the overall transfer efficiency and the exponent is a measure of how constant the transfer efficiency is with time. Since this relation suggests $TE_{AD} = t \times At^{-\beta} = At^{1-\beta}$ an exponent value $\beta < -1$ indicates a decreasing TE_{AD} with time and $\beta > -1$ indicates an increasing TE_{AD} with time. A value of $\beta = -1$ indicates TE_{AD} that is constant in time.The value of $\beta = -0.773$ found from our fit is consistent with the weakly increasing TE_{AD} with time seen in our data. The coefficient of the fit, 0.056 can be interpreted as a global parameter of the system related to the transfer efficiency rate, akin to the deposition rate. In an ideal system, all of the powder consumed is converted to film mass and is independent of time, $TE_{AD}/t = 100t^{-1}$. The TE_{AD}/t FoM has several features; 1) it utilizes many of the parameters of the system, powder mass, sweep area, and time and relates them to the final film thickness and density; 2) the data follow a simple time dependent form that is fit by a simple power-law; 3) the coefficient provides a quantitative way to assess and compare AD systems and material deposition efficiency.

Some additional features of this FoM deserves comment. The fairly weak time dependence of TE_{AD} is hinted at from the results and interpretation of Fig. 2. This points to the possibility that packing and clumping of the powder in the AC is having a significant effect on the transfer efficiency. One possible explanation is that the amount of powder exiting the nozzle changes with time. Initially, during start-up, turbulent flow causes a large amount of powder to flow. As the deposition begins, mass flow decreases as the usable portion of the powder in the AC is consumed. This is hinted at by the plot of TE_{AD}/t.

Eq. (3) merits further exploration since the form of TE_{AD}/t could depend on the time dependence of T_{film} and the mass consumption. For example, if thickness and mass consumption both depended linearly on time TE_{AD}/t should be constant in time (or a TE_{AD} linear in time). Exploration of these relationships may provide insight into further modeling and understanding film growth. In general, mass consumption and thickness could depend on several variables and have quite complicated dependences on time as hinted at in the behavior shown in Fig. 4.

3.3. Simulations of particle flow and impact

Fig. 5 shows results of a simulation of the gas flow in the NRL AD system with the nozzle set to a 10 mm standoff distance. The color bar indicates gas velocity in the *x*-direction and the black lines represent massless gas flow line tracers. In the top plot the gas is seen to exit the nozzle and pass over the substrate and mounting stage and continue into the pump. The bottom plot of Fig. 5 shows the region near the nozzle and substrate. The plot shows that the gas attains a high velocity of about 600 m/s upon exiting the nozzle. Because the pressure right at the nozzle throat is still much higher than the pressure in the deposition chamber, there is a very strong expansion of the flow coming out of the nozzle. The gas velocity decreases significantly as a normal shock-wave is formed due to the interaction of the gas with the substrate and mounting stage.

Fig. 6 shows two plots of the same configuration as shown in Fig. 5, but with spherical alumina particles (3.95 g/cm^3) of diameter 1.0, 0.75, 0.5, and 0.1 μm placed inside the nozzle at the $x = 13$ mm location shown. The top plot shows the particles initially placed toward to sidewall of the nozzle and the bottom plot shows the particles placed near the center of the nozzle. The simulation shows that only particles of diameter 0.75 μm and greater have enough inertia to break free of the flow lines and impact with the substrate. The simulation also suggests that smaller particles that are located near the center of the nozzle may approach the substrate closer and therefore may have a better chance of depositing.

Fig. 7 shows a comparable plot to Fig. 6 for a standoff distance of 7.5 mm. For particles that are placed near the sidewall of the nozzle the behavior is similar to the 10 mm standoff distance. However, for particles that start near the center of the nozzle, the 0.5 μm diameter

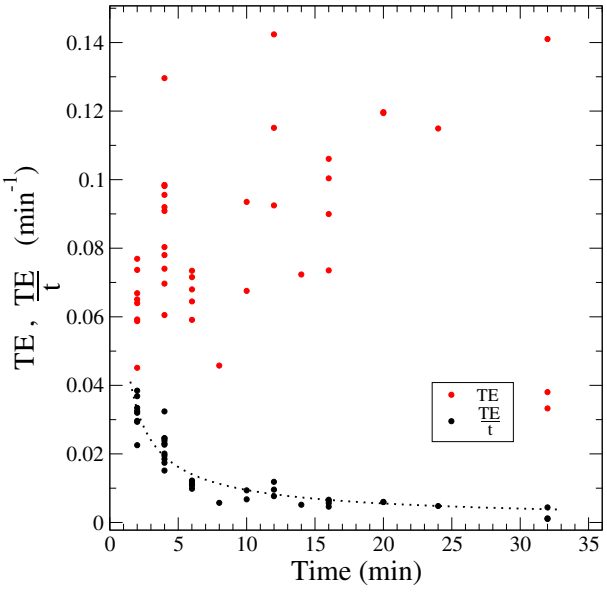

Fig. 4. A plot of the transfer efficiency (TE_{AD}) and TE_{AD}/t calculated from Eq. (3) versus time of deposition. The TE_{AD} shows large spread of values, whereas the TE_{AD}/t shows a power law dependence on time. The average TE_{AD} for all the runs was 0.082%. (For interpretation of the references to color in this figure legend, the reader is referred to the web version of this article.)

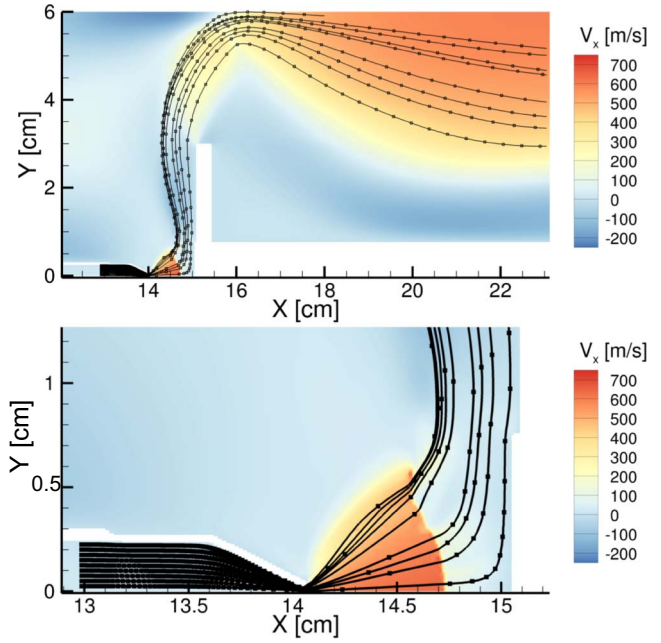

Fig. 5. Velocity map of the gas flowing out of a converging nozzle toward a substrate and mounting stage. The black lines are massless tracers indicating the flow lines of the gas. The top plot shows an expanded view of the simulation region. The bottom plot shows the region in the immediate vicinity of the nozzle and substrate highlighting the normal shockwave that occurs in the gas due to the presence of the substrate and mounting stage.

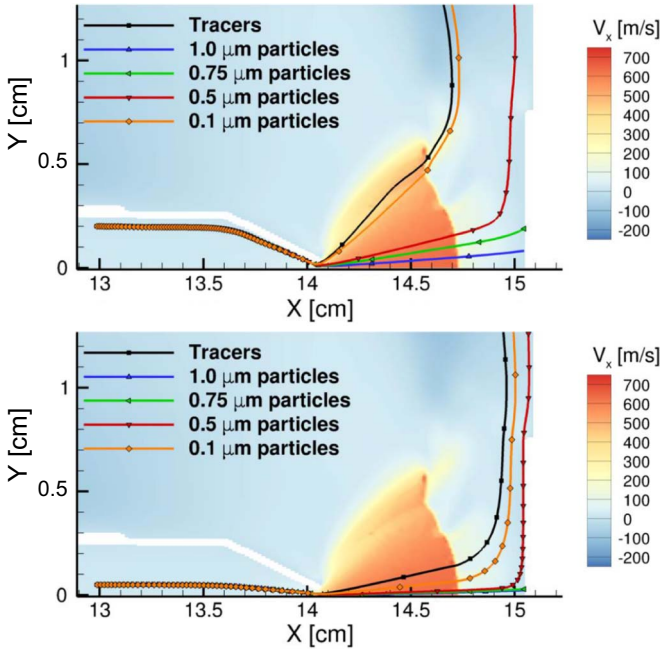

Fig. 6. Velocity map of the gas flowing out of the NRL converging nozzle toward a substrate and mounting stage at 10 mm standoff distance. Spherical particles with density 3.95 g/cm^3 and different diameters are set into the nozzle at 13 mm location near the sidewall (top) and center (bottom). The simulation suggests that particle diameter has a significant effect on whether the particle will impact the substrate.

particles will also impact the substrate with this shorter distance.

Fig. 8 contains two plots of the x velocity versus distance of each particle presented. The plot on the left is for the 10 mm standoff distance and the plot on the right is for the 7.5 mm standoff distance. The vertical dashed lines indicate the locations of the nozzle throat and substrate in Figs. 6 and 7. The solid lines are for particles starting near the center of the nozzle (bottom panel in Figs. 6 and 7) and dashed lines

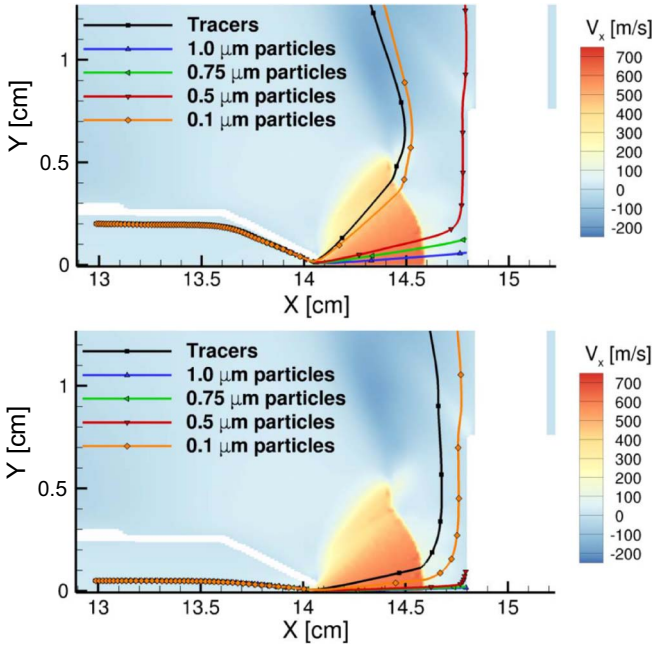

Fig. 7. Velocity map of the gas flowing out of the NRL converging nozzle toward a substrate and mounting stage at 7.5 mm standoff distance. Spherical particles with density 3.95 g/cm^3 and different diameters are set into the nozzle at 13 mm location near the sidewall (top) and center (bottom). The simulation suggests that at a shorter standoff distance smaller particles have a better chance of depositing if coming from the central portion of the nozzle.

represent particles starting near the edge of the nozzle (top panel of Figs. 6 and 7). For the 10 mm (7.5 mm) standoff the centerline particles attain a maximum velocity between 520 and 640 m/s (480–630 m/s) before entering the normal shock wave where they abruptly drop in velocity and are either carried away by the gas (as seen by movement beyond the substrate) or impact with the substrate. The impact velocities for the 10 mm (7.5 mm) standoff are 250 m/s and 120 m/s (300 m/s and 220 m/s) for the 1.0 μm and 0.75 μm, respectively. There is no apparent difference in impact velocity based on starting location within the nozzle.

There are several features of these simulations that are worth commenting. First, the impact velocity and particle sizes that impact that are found in this simulation match well with the values reported in the literature [15,20,33,34]. This suggests the simulation may be a good representation of the AD particle flow. Second, the simulation demonstrates the importance of nozzle design to focus the particles toward the nozzle center to maximize impact and therefore *TE*. Third, the simulation offers insight into the *TE* by suggesting that very small changes in particle size and location in the nozzle can have a large effect on whether the particles impact the substrate. Fourth, the effect of nozzle standoff distance appears to be significant and may partially explain the decrease in film thickness with increasing standoff distance found by Chun et al. [19] From the above points, the simulation offers several avenues to improve the *TE* of the AD process by tuning particle size and substrate distance. These results also indicate that particle size distribution may be an important factor in improving the *TE*.

To illustrate this principle we have classified particles into three size regimes as shown in Fig. 9. The black lines represent the flow lines of the gas and the circles represent the particles entrained in the gas. In Fig. 9 particle *A* is too large and is too massive, so the impact results in abrasion of the substrate with very little or no deposition occurring. Particle *B* has the correct mass to achieve deposition and particle *C* is too light to break from the gas flow lines to impact with the substrate. While the simulations presented here can provide a gauge of the lower bound (in this case 0.75 μm). Micromechanical simulations must be

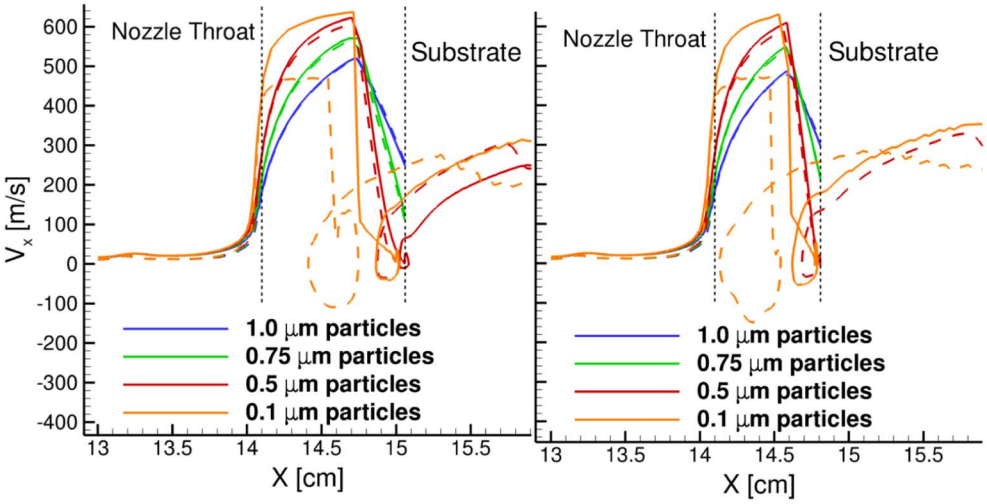

Fig. 8. X-velocity plots of the particles shown in Figs. 6 (left) and 7 (right) for starting locations near the sidewall (dashed) and near the center (solid). The nozzle throat and substrate are indicated by the vertical dashed lines. Movement past the substrate indicates impact did not occur.

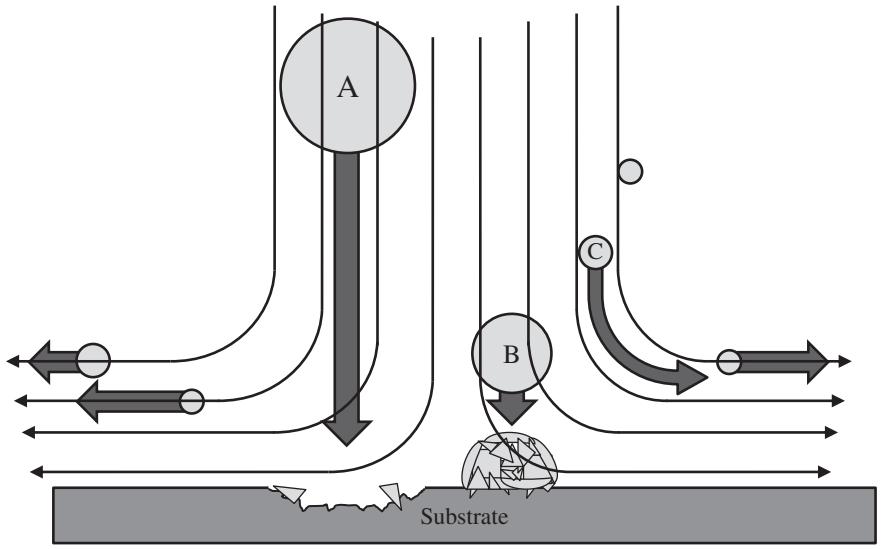

Fig. 9. A drawing representing the aerosol deposition process with gas flow consideration. The black lines represent the gas flow lines. Particle *A* is too massive to achieve deposition resulting in poor adhesion and substrate abrasion. Particle *B* has the correct mass to achieve the necessary fracture and deformation upon impact to deposit. Particle *C* does not have sufficient mass to break free from the gas flow lines and is carried away before impacting the substrate.

explored to determine the impact behavior of particle *A*. It can also be inferred from the simulations and mass consumption results that to improve TE_{AD} nozzle design must be optimized, particle size must be carefully selected, standoff distance must be selected, and the powder in the AC must be delivered at an optimal rate. These factors may be individually tuned to contribute to the final TE_{AD} FoM that can be used to assess the efficiency of the AD process.

4. Conclusion

We present results of powder mass consumption of barium hexaferrite powder over a wide range of starting powder quantities and deposition time durations. We use these data to form a transfer efficiency figure of merit for AD growth comparisons that is more accurate description of the process than those utilized currently. We find that the transfer efficiency of barium hexaferrite for the KIMS AD system was 0.08% and the transfer efficiency rate coefficient was 0.056 min^{-1} with a decay factor of -0.773. We present flow simulations of the NRL AD system using different particle sizes and standoff distances. We find that impact with the substrate strongly depends on the particle size, particle location within the nozzle, and standoff distance. We find that to improve TE_{AD} nozzle design must be optimized, particle size must be carefully selected, standoff distance must be selected, and the powder in the AC must be delivered at an optimal rate. These factors may be individually tuned to contribute to the final TE_{AD} FoM that can be used to assess the efficiency of the AD process.

Acknowledgments

Funding for this project was provided by the Office of Naval Research through the Naval Research Laboratory's 6.1 Research Program and by the Korean Institute of Material Science.

References

[1] J. Akedo, M. Ichiki, K. Kikuchi, R. Maeda, Jet moulding system for realization of three-dimensional micro-structures, Sensors Actuators A 69 (1998) 106.
[2] C. Hayashi, Ultrafine particles, J. Vac. Sci. Technol. A 5 (4, 2) (1987) 1375–1384, http://dx.doi.org/10.1116/1.574773.
[3] S. Kashu, E. Fuchita, T. Manabe, C. Hayashi, Deposition of ultra fine particles using a gas-jet, Jpn. J. Appl. Phys. 2 Lett. 23 (12) (1984) L910–L912, http://dx.doi.org/10.1143/JJAP.23.L910.
[4] J. Ryu, J.-J. Choi, B.-D. Hahn, D.-S. Park, W.-H. Yoon, Ferroelectric and piezoelectric properties of 0.948(K(0.5)Na(0.5))NbO(3)-0.052LiSbO(3) lead-free piezoelectric thick film by aerosol deposition, Appl. Phys. Lett. 92 (012905) (2008), http://dx.doi.org/10.1063/1.2828892.
[5] B.-D. Hahn, D.-S. Park, J.-J. Choi, J. Ryu, W.-H. Yoon, J.-H. Choi, J.-W. Kim, C.-W. Ahn, H.-E. Kim, B.-H. Yoon, I.-K. Jung, Osteoconductive hydroxyapatite coated PEEK for spinal fusion surgery, Appl. Surf. Sci. 283 (2013) 6–11, http://dx.doi.org/10.1016/j.apsusc.2013.05.073.
[6] S.D. Johnson, F.J. Kub, C.R. Eddy Jr, ZnS/diamond composite coatings for infrared transmission applications formed by the aerosol deposition method, Proc. of

SPIE 8708 (2013) (87080T-1).
[7] Y. Kato, S. Sugimoto, J. Akedo, Magnetic properties and electromagnetic wave suppression properties of Fe-ferrite films prepared be aerosol deposition method, Japan J. Applied Phys. 47 (2008) 2127.
[8] S.D. Johnson, C.M. Gonzalez, V. Anderson, Z. Robinson, H.S. Newman, S. Shin, S. Qadri, Magnetic and structural properties of sintered bulk pucks and aerosol deposited films of Ti-doped barium hexaferrite for microwave absorption applications, J. Appl. Phys. 122 (024901) (2017), http://dx.doi.org/10.1063/1.4991808.
[9] S.D. Johnson, E.R. Glaser, S.-F. Cheng, H.S. Newman, M.J. Tadjer, F.J. Kub, C.R. Eddy Jr, Aerosol deposition of yttrium iron garnet for fabrication of ferrite-integrated on-chip inductors, IEEE T. Magn. 51 (05) (2015) 1–6, http://dx.doi.org/10.1109/TMAG.2014.2369376.
[10] H.S. Ryu, T.S. Lim, J. Ryu, S.-H. Hong, Corrosion protection performance of ysz coating on aa7075 aluminum alloy prepared by aerosol deposition, J. Electrochem. Soc. 160 (1) (2013) C42–C47, http://dx.doi.org/10.1149/2.038302jes.
[11] D. Hanft, J. Exner, M. Schubert, T. Stoecker, P. Fuierer, R. Moos, An overview of the aerosol deposition method: process fundamentals and new trends in materials applications, J. Ceramic Sci. Technol. 6 (3) (2015) 147–181, http://dx.doi.org/10.4416/JCST2015-00018.
[12] J. Akedo, Room temperature impact consolidation (RTIC) of fine ceramic powder by aerosol deposition method and applications to microdevices, J. Therm. Spray Techn. 17 (2) (2008) 181–198, http://dx.doi.org/10.1007/s11666-008-9163-7.
[13] R. Dykhuizen, M. Smith, Gas dynamic principles of cold spray, J. Therm. Spray Technol. 7 (2) (1998) 205–212, http://dx.doi.org/10.1361/105996398770350945.
[14] A. Papyrin, V. Kosarev, S. Klinkov, A. Alkhimov, V. Fomin, Cold Spray Technology, 1st edition, Elsevier Science, 2006.
[15] M. Lebedev, J. Akedo, K. Mori, T. Eiju, Simple self-selective method of velocity measurement for particles in impact-based deposition, J. Vac. Sci. Technology A 18 (2000) 563.
[16] H. Katanoda, M. Fukuhara, N. Iino, Numerical simulation on impact velocity of ceramic particles propelled by supersonic nitrogen gas flow in vacuum chamber, Mater. Trans. 48 (6) (2007) 1463–1468, http://dx.doi.org/10.2320/matertrans.T-MRA2007833.
[17] J.-J. Park, M.-W. Lee, S.S. Yoon, H.-Y. Kim, S.C. James, S.D. Heister, S. Chandra, W.-H. Yoon, D.-S. Park, J. Ryu, Supersonic nozzle flow simulations for particle coating applications: effects of shockwaves, nozzle geometry, ambient pressure, and substrate location upon flow characteristics, J. Therm. Spray Techn. 20 (3) (2011) 514–522, http://dx.doi.org/10.1007/s11666-010-9542-8.
[18] M.W. Lee, J.J. Park, D.Y. Kim, S.S. Yoon, H.Y. Kim, D.H. Kim, S.C. James, S. Chandra, T. Coyle, J.H. Ryu, W.H. Yoon, D.S. Park, Optimization of supersonic nozzle flow for titanium dioxide thin-film coating by aerosol deposition, J. Aerosol Sci. 42 (11) (2011) 771–780, http://dx.doi.org/10.1016/j.jaerosci.2011.07.006.
[19] D.-M. Chun, J.-O. Choi, C.S. Lee, S.-H. Ahn, Effect of stand-off distance for cold gas spraying of fine ceramic particles ($< 5\,\mu m$) under low vacuum and room temperature using nano-particle deposition system (NPDS), Surf. Coat. Technol. 206 (8–9) (2012) 2125–2132, http://dx.doi.org/10.1016/j.surfcoat.2011.09.043.
[20] K. Mihara, T. Hoshina, H. Takeda, T. Tsurumi, Controlling factors of film-thickness in improved aerosol deposition method, J. Ceram. Soc. Jpn. 117 (1368) (2009) 868–872, http://dx.doi.org/10.2109/jcersj2.117.868.
[21] J. Akedo, M. Lebedev, Powder preparation in aerosol deposition method for lead zirconate titanate thick films, Jpn. J. Appl. Phys. Part 1 41 (11B) (2002) 6980–6984, http://dx.doi.org/10.1143/JJAP.41.6980 (13th IEEE International Symposium on Applications of Ferroelectrics, Nara, Japan, May 28–June 01, 2002).
[22] L. Schiller, A. Naumann, Uber die grundlegenden berechungen bei der schwerkraftaufbereitung, Ver, Deut. Ingr. 77 (1933) 318.
[23] J. Boris, D. Book, Flux-corrected transport. I. SHASTA, a fluid transport algorithm that works, J. Comput. Phys. 11 (1) (1973) 38.
[24] J. Boris, A. Landsberg, E. Oran, J. Gardner, LCPFCT - a flux-corrected transport algorithm for solving generalized continuity equations, Nrl Technical Report nrl/mr/6410-93-7192, Naval Research Laboratory, Washington DC, 1973.
[25] G. Agrawal, A. Sussman, J. Saltz, An integrated runtime and compile-time approach for parallelizing structured and block structure applications, IEEE Trans. Parallel Distrib. Syst. 6 (7) (1995) 747.
[26] A. Landsberg, J. Boris, The virtual cell embedding method - a simple approach for building complex geometries, 1997, 13th Computational Fluid Dynamics Conference, Snowmass Village, CO, USA, 1997, , http://dx.doi.org/10.2514/6.1997-1982.
[27] S.D. Johnson, E.R. Glaser, F. Kub, C.R. Eddy Jr, Formation of thick dense yttrium iron garnet films using aerosol deposition, J. Vis. Exp. 99 (2015) e52843, http://dx.doi.org/10.3791/52843.
[28] S.D. Johnson, E.R. Glaser, S.-F. Cheng, F. Kub, C.R. Eddy Jr, Characterization of as-deposited and sintered yttrium iron garnet thick films formed by aerosol deposition, Appl. Phys. Express 7 (2014) 035501.
[29] J.-H. Park, D.-S. Park, B.-D. Hahn, J.-J. Choi, J. Ryu, S.-Y. Choi, J. Kim, W.-H. Yoon, C. Park, Effect of raw powder particle size on microstructure and light transmittance of alpha-alumina films deposited by granule spray in vacuum, Ceram. Int. 42 (2, B) (2016) 3584–3590, http://dx.doi.org/10.1016/j.ceramint.2015.11.009.
[30] Y. Park, D.-S. Park, S.D. Johnson, W.-H. Yoon, B.-D. Hahn, J.-J. Choi, J. Ryu, J.-W. Kim, C. Park, Effect of gas flow rates and nozzle throat width on deposition of α-alumina films of granule spray in vacuum, J. Eur. Ceram. Soc. 37 (2017) 2667–2672, http://dx.doi.org/10.1016/j.jeurceramsoc.2017.02.021.
[31] K. Shinoda, J. Colmenares-Angulo, A. Valarezo, S. Sampath, Effect of deposition rate on the stress evolution of plasma-sprayed yttria-stabilized zirconia, J. Therm. Spray Technol. 21 (6) (2012) 1224–1233, http://dx.doi.org/10.1007/s11666-012-9807-5 (5th International Workshop on Suspension and Solution Thermal Spraying, Tours, FRANCE, OCT 03-05, 2011).
[32] K. Kennedy, Development of proposed standard test method for spray painting transfer efficiency: volume 1 - laboratory development, Technical Report for the US Environ. Protection Agency, Air and Energy Engineering Research Laboratory, Research Triangle Park, NC, 1988, https://nepis.epa.gov/Exe/ZyPURL.cgi?Dockey=9100KKEV.txt.
[33] S.D. Johnson, E.R. Glaser, S.F. Cheng, J. Hite, Dense nanocrystalline yttrium iron garnet films formed at room temperature by aerosol deposition, Mat. Res. Bull. 76 (2015) 365.
[34] J.-M. Oh, S.-M. Nam, Role of surface hardness of substrates in growing BaTiO3 thin films by aerosol deposition method, Jpn. J. Appl. Phys. 48 (09KA07) (2009), http://dx.doi.org/10.1143/JJAP.48.09KA07.